# Effect of interfaces on the dielectric response of a $SrTiO_3$ layer between metallic oxide electrodes

Yu. A. Boikov,[1,2] E. Olsson,[1] and T. Claeson[1]
[1]*Microtechnology and Nanoscience, Chalmers University of Technology, SE-41296 Gothenburg, Sweden*
[2]*Ioffe Physico-Technical Institute, Russian Academy of Science, 194021 St. Petersburg, Russia*
(Received 21 March 2006; published 26 July 2006)

The temperature dependence of the dielectric permittivity $\varepsilon$ of an 800 nm thick $SrTiO_3$ layer in epitaxial $SrRuO_3/SrTiO_3/SrRuO_3$ and $YBa_2Cu_3O_{7-\delta}/SrTiO_3/SrRuO_3$ heterostructures followed the relation $\varepsilon^{-1}=\varepsilon_0^{-1}C_0^{-1}(T-T_{CW})+\varepsilon_I^{-1}$, where $C_0$ and $T_{CW}$ are the Curie constant and the Curie-Weiss temperature for the strontium titanate bulk crystal, respectively. The effective dielectric constant is lower than the bulk value due to the interfaces of the $SrTiO_3$ film to its electrodes as given by $\varepsilon_I$. The $\varepsilon_I$ was diminished roughly 2.5 times when the top $SrRuO_3$ electrode in the trilayer was replaced by one of $YBa_2Cu_3O_{7-\delta}$. The capacitances $C_i$ per unit area of the $SrRuO_3/SrTiO_3$ and $YBa_2Cu_3O_{7-\delta}/SrTiO_3$ interfaces were 8.2 and 2.3 $F/cm^2$, respectively. Characteristic penetration depths $L$ of the electric field into the $SrRuO_3$ and $YBa_2Cu_3O_{7-\delta}$ electrodes were extracted from the $C_i$s and are several times larger than corresponding data estimated from free electron type models of metals. A diminished charge carrier density in the electrode very close to the interface is a likely reason for the enhanced $L$.

DOI: 10.1103/PhysRevB.74.024114 PACS number(s): 77.22.Ch, 77.55.+f, 77.80.Dj, 77.84.Dy

## I. INTRODUCTION

The dielectric response of a ferroelectric layer in a heterostructure depends on the structure and electron configuration at the interfaces to its metallic electrodes. The use of thin epitaxial films of perovskite-type metallic oxides, like $SrRuO_3$ (SRO), $La_{1-x}(Ca,Sr)_xMnO_3$ (LCMO, LSMO), or $YBa_2Cu_3O_{7-\delta}$ (YBCO), as electrodes promotes the growth of a well preferentially oriented ferroelectric $(Ba,Sr)TiO_3$ layer and sharp interface boundaries between the layer and its electrodes.[1–3] That results in the enhanced dielectric permittivity, $\varepsilon$, of the ferroelectric film and promotes Curie-Weiss behavior,[4] which is not common in the case of a noble metal electrode. The effect of the interfaces on $\varepsilon$ of a structurally perfect ferroelectric film at temperatures just above the ferroelectric-paraelectric phase transition point is markedly enhanced because of the large $\varepsilon$.

Perovskite-type ruthenates, manganites, and high-$T_c$ superconducting cuprates differ in unit cell parameters as well as in electronic and magnetic properties. Thus, the choice of electrode material is important for most applications of the nonlinear ferroelectrics. However, no detailed comparative study of the impact of electrode interfaces on $\varepsilon$ of the ferroelectric layer has been done up till now.

We will report on the influence of electrode and ferroelectric interfaces on the effective dielectric permittivity of the ferroelectric layer in between two SRO electrodes. To gain further insight, the top SRO electrode was replaced by YBCO. A substantial part of the parallel plate capacitance of the heterostructures of SRO/STO/SRO or YBCO/STO/SRO is due to the interfaces.

## II. EXPERIMENT

Laser ablation (KrF, $\lambda=248$ nm, $\tau=30$ ns) was used to grow the bottom metallic oxide electrode of (45 nm) SRO at the surface of a $(001)(LaAlO_3)_{0.3}+(Sr_2AlTaO_6)_{0.7}$ (LSATO) substrate. A ($d=800$ nm) STO layer was subsequently deposited on the SRO electrode and, finally, a (45 nm) thick top film of SRO or YBCO was condensed on the ferroelectric film. The substrate temperature was fixed at 780 °C during the growth of the ferroelectric and conducting oxide films. They were all grown in an oxygen atmosphere, $p_O=0.3$ mbar.

X-ray diffraction (Philips X'pert MRD, Cu $K\alpha1$, $\omega/2\theta$ scans, and $\phi$ scans, rocking curves) was used to investigate phase purity, orientation, and lattice parameters in the films of the multilayers. We traced $\omega/2\theta$ x-ray scans ($2\theta=20-120°$) when incident and scattered beams were normal to (001) or (101)LSATO.

The atomic structure of the interfaces in the multilayer heterostructure was determined using transmission electron microscopy (TEM). The cross-section TEM specimens were prepared using mechanical polishing and final ion beam thinning to electron transparency. The TEM was carried out at room temperature using a CM200 supertwin field emission gun TEM operated at 200 kV.

Photolithography and ion milling (Ar, 500 V, 0.2 mA) were used to form square contact pads ($S=100\times100$ $\mu m^2$) on the top electrodes and in openings in the intermediate STO layer to contact the bottom (common) electrode.

The capacitance, $C$, of the formed parallel plate capacitor was measured by an hp 4263A *LCR* meter in a frequency interval of 1–100 kHz, with and without bias voltage $V_b=\pm2.5$ V. The measured $C$ was used to determine the effective dielectric permittivity $\varepsilon$ of the intermediate STO layer (assuming a parallel plate capacitor). Resistance $R$ of the bottom and top SRO (YBCO) electrodes was measured in a van der Pauw geometry by the same *LCR* meter. Resistivity $\rho$ was then calculated as $\rho=\pi Rd_0/\ln 2$,[5] where $d_0$ is the thickness of the electrode.

## III. RESULTS

The mismatch $m$ in lattice parameters of the LSATO (pseudocubic unit cell, $a_1=3.868$ Å)[6] and SRO (pseudocu-

 

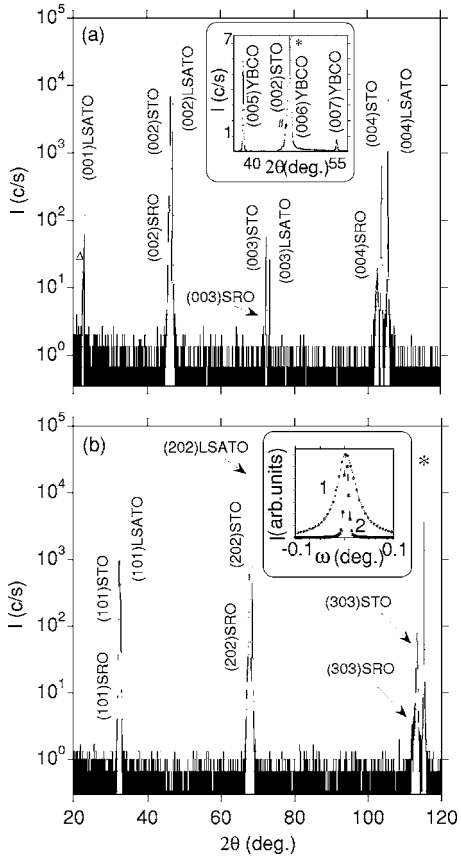


FIG. 1. (a) X-ray scan ($\omega/2\theta$, Cu $K\alpha 1$) for the SRO/(800 nm)STO/SRO/(001)LSATO heterostructure measured when the substrate plane was normal to the plane formed by incident and scattered x-ray beams. Δ, overlapping (001)SRO and (001)STO peaks. The inset shows a fragment of the $\omega/2\theta$ x-ray scan for the YBCO/(800 nm)STO/SRO/(001)LSATO heterostructure. # and *, (002)SRO and (002)LSATO peaks, respectively. (b) X-ray scan for the same heterostructure measured when the (101)LSATO plane was normal to the plane formed by incident and scattered x-ray beams. *, (303)LSATO peak. The inset plots rocking curves for (002)STO (1) and (002)LSATO (2) reflections from the SRO/(800 nm)STO/SRO/(001)LSATO heterostructure.

bic, $a_2$=3.927 Å)[7] is positive and about 1.5% [$m=(a_L-a_S)/a_S$, where $a_L$ and $a_S$ are lattice parameters of the layer and substrate, respectively]. In the case of SRO on STO, $m$ is positive ~0.5% (STO has a cubic unit cell, $a_3$=3.905 Å),[8] but for YBCO/STO, $m$ is negative ~1.5% (parameters of the orthorhombic unit cell of the YBCO are $a$=3.82 Å, $b$=3.89 Å, $c$=11.68 Å).[9] Thermal expansion coefficients of the STO, SRO, YBCO, and LSATO match each other reasonably well in the temperature interval of interest.[9,10]

The x-ray scans for SRO/STO/SRO and YBCO/STO/SRO heterostructures peaked at angles corresponding to reflections from the ferroelectric layer, the electrodes and the substrate, see Figs. 1(a) and 1(b). The films of the heterostructures were well in-plane and out-of-plane preferentially oriented, as follows from the measured x-ray $\omega/2\theta$ scans and $\phi$ scans.

The in-plane lattice parameter of the STO layers in the grown multilayers was roughly the same as the out-of-plane

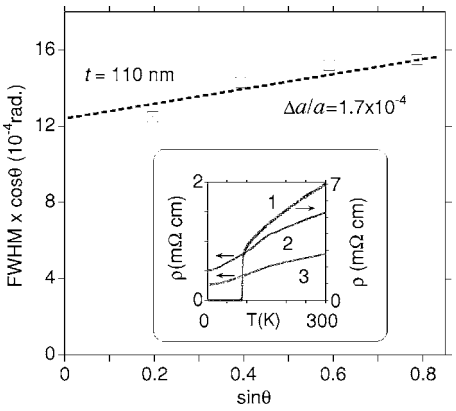


FIG. 2. Bragg peak FWHM as a function of the diffraction angle for the (800 nm) STO layer in the SRO/STO/SRO/(001)LSATO heterostructure. The inset shows temperature dependencies of the resistivity of YBCO (1) and SRO (2) electrodes grown on an (800 nm)STO/SRO/(001)LSATO, and an SRO film (3) formed on (001)LSATO.

one (3.908±0.005 Å), both agree reasonably well with the lattice parameter of a stoichiometric STO single crystal. Hence, mechanical stresses in the ferroelectric layer were relaxed to a large extent.

To estimate strain distribution in the STO layer the variation of the FWHM (width of the peak at half of maximum) of the (00$n$)STO peaks in the x-ray scans was plotted as a function of the sin $\theta$. According to[11]

$$\mathrm{FWHM} = 0.9\lambda_0/(t\cos\theta) + 2\tan\theta\Delta a/a, \qquad (1)$$

where $a$ is the lattice parameter, $t$ the grain size, and $\lambda_0$ =1.5406 Å, the x-ray wavelength. FWHM cos $\theta$ vs sin $\theta$ for the STO layer in SRO/STO/SRO is plotted in Fig. 2. From the slope of the line we get an effective strain $\Delta a/a \approx 1.7 \times 10^{-4}$ in the ferroelectric layer. The $\Delta a/a$ determined for STO in SRO/STO/SRO agree well with the corresponding data for a $(Ba,Sr)TiO_3$ layer.[12,13] FWHMs of the rocking curves for the (002)STO x-ray peak from the heterostructures of SRO/STO/SRO and YBCO/STO/SRO were the same [≈0.06°, inset Fig. 1(b)].

The effective out-of-plane lattice parameter (3.95±0.01 Å) of the SRO electrodes was substantially larger than the in-plane one (3.91±0.01 Å). (The x-ray peaks from the two metallic oxide electrodes overlap and limit the precision in the determination of the unit cell parameters in the top and bottom layers in the SRO/STO/SRO.) Both SRO electrodes were in-plane compressively stressed due to the positive mismatch in lattice parameters between SRO and LSATO (STO). The YBCO electrode grown on the STO/SRO/LSATO was well $c$ axis preferentially oriented ($c$ =11.68±0.005 Å); see the inset in Fig. 1(a). Separate, small $a$ axis oriented particles were detected by an atomic force microscope on the surface of the YBCO/STO/SRO heterostructure.

The TEM investigations confirmed the epitaxial growth of the SRO and STO films combined into the multilayer heterostructure [see Figs. 3(a) and 3(b)]. Strain-induced two di-

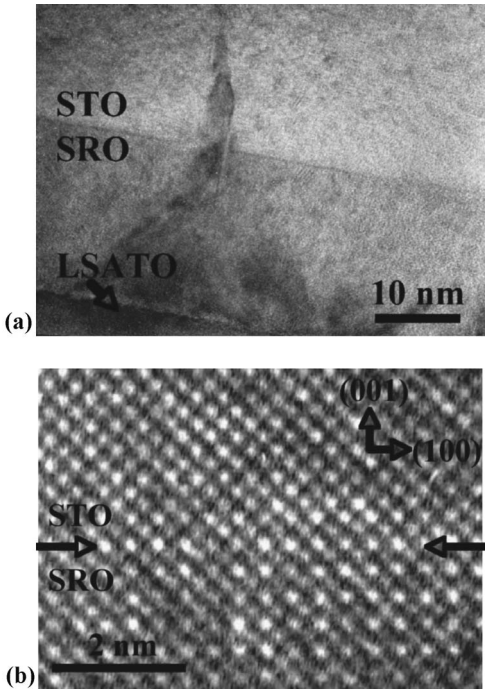


FIG. 3. (a) Low magnification electron microscopy image of the cross section of a SRO/STO/SRO/LSATO heterostructure near around the bottom SRO/STO interface. A characteristic two dimensional (probably dislocation wall) defect in the electrode is clearly detectable. (b) High resolution transmission electron micrograph of a cross-sectional image of the same interface. The interface is marked by arrows.

mensional defects in the bottom SRO layer are clearly detectable in the TEM images. The defects nucleated at the SRO/LSATO interface and propagated through the whole thickness of the bottom metallic oxide electrode at an angle of ~45° to the substrate plane [see Fig. 3(a)]. The lateral distance between observed defects in the STO layer was about 100 nm. That agrees well with $t \approx 110$ nm (effective grain size) determined from the intersection of the straight line (FWHM $\times \cos\theta$ vs $\sin\theta$ in Fig. 2) with the ordinate axis. The interfaces between the ferroelectric layer and electrodes were free from second phase inclusions as follows from high resolution TEM image shown in Fig. 3(b). Data on the microstructure of the YBCO/STO interfaces were presented in Ref. 2.

Temperature dependencies of the resistivity of the top SRO and YBCO electrodes in the trilayer heterostructures as well as of the (80 nm) SRO layer grown on (001)LSATO are shown in the inset of Fig. 2. Ferromagnetic ordering of spins on $Ru^{+4}$ ions at $T \approx 160$ K are clearly marked by the change of slopes in the $\rho(T)$ curves for the SRO layers. Strain induced defects of structure are a likely reason for the measured larger resistivities of the top SRO layer in the SRO/STO/SRO and of the SRO/LSATO film as compared with that of a bulk strontium ruthenate crystal. The crystallinity of the layers in a multilayer heterostructure is typically degraded with the increase of their number and thickness because of the accumulation of defects. That partly explains the difference in $\rho$ between the top SRO electrode in SRO/STO/SRO/LSATO and the SRO/LSATO film. The superconducting transition temperature ($\rho=0$) for the top YBCO electrode in YBCO/STO/SRO was ~87 K.

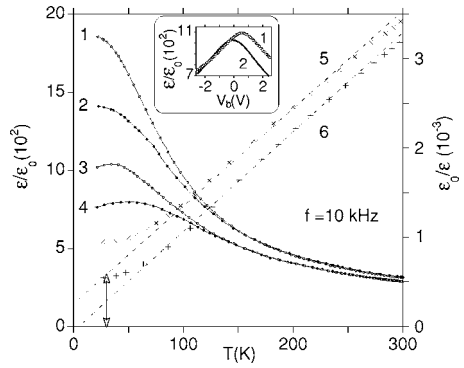


FIG. 4. Temperature dependencies of the $\varepsilon/\varepsilon_0$ (1–4) and $\varepsilon_0/\varepsilon$ (5,6) for the (800 nm) STO layer in the SRO/STO/STOO/LSATO (1,2,6) and YBCO/STO/STOO/LSATO (3–5) heterostructures. The biases for (1,3,5,6) $V_b=0$ V; for (2,4) $V_b=-2$ V. Tangents of the curves 5 and 6 at $T=70-270$ K are marked by dashed lines. $\varepsilon_0/\varepsilon_I(T_{CW}=30\ \text{K})$ for the STO layer in the YBCO/STO/SRO/LSATO heterostructure is marked by a double sided arrow ($f=10$ kHz). The inset plots $\varepsilon/\varepsilon_0(V_b)$ (1) and $\varepsilon/1.8\times\varepsilon_0(V_b)$ (2) dependencies for the (800 nm) STO layer in the YBCO/STO/SRO/(001)LSATO and SRO/STO/SRO/(001)LSATO heterostructures, respectively ($T=40$ K).

The dielectric permittivity of the STO layer in the SRO/STO/SRO and YBCO/STO/SRO heterostructures was dispersionless in the used frequency range. A response of $\varepsilon$ of the STO layer on an external electric field was detectable at $T<100$ K (see Fig. 4). The $\varepsilon/\varepsilon_0(V_b)$ curves for the STO layer in the SRO/STO/SRO heterostructure were roughly symmetric relative to the point $V_b=0$ when measured at $T<77$ K. In contrast to that, the maximum in the $\varepsilon/\varepsilon_0(V_b)$ dependence for the STO layer in the YBCO/STO/SRO heterostructure was shifted ($V_M \approx 0.6$ V) towards positive $V_b$ (see the inset in Fig. 4). That shows an internal electric field of $E_{\text{int}}=V_M/d \approx 7.5$ kV/cm in the ferroelectric layer of the YBCO/STO/SRO heterostructure. A likely reason is the difference in work functions of the top YBCO (Ref. 14) and bottom SRO (Ref. 15) electrodes.

## IV. ANALYSIS

Temperature dependencies of $\varepsilon$ for the STO layer in SRO/STO/SRO/LSATO and YBCO/STO/SRO/LSATO heterostructures are shown in Fig. 4. The permittivity of the STO layer in YBCO/STO/SRO was substantially smaller than that of the ferroelectric layer in SRO/STO/SRO (markedly so at low temperatures). They are of high quality as, in the temperature interval 70–270 K, $\varepsilon_0/\varepsilon(T)$ curves for the STO layer in both types of trilayers were well described by the relation

$$\varepsilon^{-1} = \varepsilon_0^{-1} C_0^{-1} (T - T_{CW}) + \varepsilon_I^{-1}, \qquad (2)$$

where $C_0 \approx 9\times 10^4$ K and $T_{CW}=30$ K are the same as the values of the Curie constant and the Curie-Weiss temperature

for bulk crystals of strontium titanate.[16,17] The first term in the right hand side of Eq. (2) is due to the capacitance induced by the intermediate ferroelectric layer ($C_f$) in the parallel plate capacitance structure, but the second one to the capacitance from the STO/electrode interfaces ($C_{\text{int}}$). $C_f$ and $C_{\text{int}}$ are connected in series and the measured $C=(C_f \times C_{\text{int}})/(C_f+C_{\text{int}})$. $C_f$ may be assumed to be the same in both types of the investigated film capacitors as the slope of the $\varepsilon_0/\varepsilon(T)$ dependencies are the same (at 70–270 K) for both SRO/STO/SRO and YBCO/STO/SRO, the widths of the corresponding rocking curves of the (002)STO x-ray peaks are identical, and the same processing conditions are used during the growth of the multilayers. $C_{\text{int}}$ is large, temperature and electric field independent. It is tempting to relate it to electric field penetration[18] into the oxide metallic electrodes.

$\varepsilon_{\text{I}}$ was about $3700\varepsilon_0$ (cf. curve 6 in Fig. 4) for the SRO/STO/SRO heterostructure. Using this value, we estimate $C_{\text{int}}$ as 0.4 nF and the effective nominal capacitance per area of STO/SRO interface (capacitance per square centimeter) as $C_i=2\times\varepsilon_{\text{I}}/d\approx 8.2\ \mu\text{F/cm}^2$ (assuming identical electronic parameters of the top and bottom interfaces in the heterostructure). This value is comparable to that for noble metal (Pt, Au,…) electrodes in contact with dielectrics[18] and to the nominal capacitance ($\sim 2.6\ \mu\text{F/cm}^2$) of an STO/$La_{0.67}Ca_{0.33}MnO_3$ interface measured at $T<250$ K.[19] However, a value of $C_i$ roughly one order of magnitude larger was estimated for the SRO/BSTO interface in Ref. 1.

The interface capacitance can be modeled as due to a field penetrating into the electrode. The penetration length should be small in a good metal but can be considerably larger if the density of charge carriers becomes small. The capacitance per unit area of the metal/dielectric interface induced by electric field penetration into the conducting electrode may be written as[18]

$$C_M = \varepsilon_M/2.3L_M, \tag{3}$$

where $L_M$ is the characteristic length of the electric field penetrating into the electrode and $\varepsilon_M$ is the permittivity of the latter. We did not find literature data on the low frequency ($f<1$ MHz) dielectric permittivity of the SRO. According to Cox *et al.*,[20] the high frequency permittivity $\varepsilon_\infty$ of SRO is about 5 $\varepsilon_0$ (the value agrees reasonably well with those for other conducting perovskite-type oxides[21,22]). We used Eq. (3), nominal interface capacitance $C_i=8.2\ \mu\text{F/cm}^2$, and $\varepsilon_\infty=5\ \varepsilon_0$ to estimate the characteristic length $L_{\text{SRO}}$ of electric field penetrating into the SRO electrode. That gave us $L_{\text{SRO}}\approx 0.23$ nm. This will be compared with the corresponding value derived from basically a free electron model.

According to Ref. 18, the dependence of $L_M$ on electronic parameters of the electrode may be expressed by the equation

$$L_M^2 = 2\varepsilon_M E_F/3n_0e^2, \tag{4}$$

where $n_0$ is the electron density, $e$ is the electron charge, and $E_F$ is the Fermi energy. (The $L_M$ was multiplied by a factor of $2/\sqrt{3}$ suggested by Simmons.[23]) Stoichiometric SRO possesses one of the largest charge carrier densities among perovskite-type oxide metals, $n_{\text{SRO}}\approx 2\times 10^{22}\ \text{cm}^{-3}$.[20] Using the relation between the Fermi energy and electron density, $E_F=(\hbar^2/2m^*)(3\pi^2 n_{\text{SRO}})^{2/3}$,[24] and the value of the effective mass of electrons in SRO, $m^*=3.6m_0$,[20] we get $L_{\text{SRO}}=0.37\sqrt{\varepsilon'_{\text{SRO}}}$ Å, where $\varepsilon'_{\text{SRO}}$ is the relative dielectric constant of SRO. If $\varepsilon'_{\text{SRO}}$ is equal to 5, the $L_{\text{SRO}}$ is about 0.08 nm. Thus, the estimate of $L_{\text{SRO}}$ from relation (4) is roughly 3 times smaller than that determined from the $\varepsilon_0/\varepsilon(T)$ curve and Eq. (3).

A likely reason for the enhanced characteristic penetration length of the electric field penetration into the SRO films in the SRO/STO/SRO heterostructure is a degradation of the electron density in the metallic oxide electrode at the interface. (Strictly speaking, $L_{\text{SRO}}$ is determined by $n_{\text{SRO}}$ in a nanometer thick sublayer of the electrode adjacent to the STO/SRO interface). The density of mobile electrons in SRO is quite sensitive to doping (stoichiometry) and unit cell distortions. The latter affect the delicate balance between competing Sr-O and Ru-O bonds which determine the intensity of electron exchange between ruthenium ions through oxygen orbitals.[20] Both a disturbance of the stoichiometry and mechanical stresses may be responsible for the degraded $n_{\text{SRO}}$ in the SRO electrode near the SRO/STO boundary.

An appreciable Ti diffusion from an STO substrate into an SRO film during heat treatment at $T\approx 700\ ^\circ\text{C}$ was detected by secondary ion mass spectroscopy.[25] The diffusion was accompanied by a pronounced decrease of conductance (charge carrier density) within a 5 nm thick sublayer of the SRO film near the film/substrate interface. Clear detected by TEM two dimensional defects in the SRO and STO layers of the SRO/STO/SRO heterostructure may enhance interdiffusion of components between SRO electrodes and the STO ferroelectric layer.

The unit cells of both the bottom and top SRO electrodes were substantially distorted because of biaxial compressive stresses induced by the substrate and the ferroelectric layer, compare the x-ray measurements. In-plane shrinkage and out-of-plane expansion of the unit cells have to be accompanied by a change in the relative tilting of the corner-shared $RuO_6$. That strongly affects superexchange interaction, which in turn affects electronic parameters of the SRO.[26] Furthermore, mechanical stresses acting during nucleation of the perovskite-type oxide layer can induce distortion of the stoichiometry by a formation of vacancies in oxygen and/or cation sublattices.[27]

The substantial drop of $\varepsilon$ of the STO layer when the top SRO electrode was replaced by YBCO is due to a change of the effective capacitance of the top electrode/STO interface. As seen from the data in Fig. 4, an internal electric field of 7.5 kV/cm cannot be responsible for the degradation of the dielectric permittivity of the STO layer in the YBCO/STO/SRO heterostructure even at $T<100$ K. At higher temperatures, $\varepsilon$ was independent of the applied field of $E<30$ kV/cm. The $\varepsilon_{\text{I}}$ estimated for the YBCO/STO/SRO heterostructure from the temperature dependence of $\varepsilon^{-1}$ is about $1650\varepsilon_0$ (see Fig. 4), less than half the value for SRO/STO/SRO. Using this value, we get $C_{\text{int}}\approx 0.18$ nF and assuming $C_i=8.2\ \mu\text{F/cm}^2$ for the STO/SRO interface, a value of $2.3\ \mu\text{F/cm}^2$ is derived for the nominal capacitance of the YBCO/STO film boundary in the YBCO/STO/SRO hetero-

TABLE I. Estimates of the electric field penetration depth at the interface between $SrTiO_3$ and a metal electrode.

| | $\epsilon_1/\epsilon_0$ | $C_i$ ($\mu$F/cm$^2$) | $\epsilon_M$ | $L_M$ from $C_i$ (nm) | $n_0$ (cm$^{-3}$) | $L_M$ from $n_0$ (nm) |
|---|---|---|---|---|---|---|
| SRO/STO[a] | 3700 | 8.2 | 5 | 0.23 | $2\times10^{22}$ | 0.08 |
| YBCO/STO[a] | 1650 | 2.3 | 4 | 0.67 | $4\times10^{21}$ | 0.21 |
| STO/LCMO[b] | | 2.6 | 8.5 | 1.2 | $6\times10^{21}$ | 0.16 |
| STO/LSMO[c] | 2200 | 3.9 | | | | |
| Ag/STO[d] | | | 1 | | $6\times10^{22}$ | 0.05 |

[a]This work.
[b]Reference 19.
[c]Reference 30.
[d]Reference 18.

structure. This value is 3.5 times less than the corresponding one for STO/SRO. From relation (3), $C_i=2.3\ \mu\mathrm{F/cm}^2$ and $\varepsilon_\infty\approx4\varepsilon_0$ (for stoichiometric YBCO when the field is applied along the $c$ axis[21]) we estimate the electric field penetration depth along the $c$ axis as $L_{\mathrm{YBCO}}\approx0.67$ nm.

Using relation (4), a charge carrier density of $p_{\mathrm{YBCO}}=4.1\times10^{21}$ cm$^3$ and an effective mass $m^*=5m_0$ (both $p_{\mathrm{YBCO}}$ and $m^*$ were determined for (001) plane transport in the YBCO film[28]) we get $L_{\mathrm{YBCO}}=1.07\sqrt{\varepsilon'_{\mathrm{YBCO}}}$Å. If the relative dielectric permittivity of the YBCO is 4, $L_{\mathrm{YBCO}}\approx0.21$ nm. This is about three times smaller than the corresponding value determined from $\varepsilon(T)$ of the STO layer in the YBCO/STO/SRO heterostructure. The main reason for the enhanced $L_{\mathrm{YBCO}}$ (as for $L_{\mathrm{SRO}}$) is the diminished charge carrier density in a sublayer of the YBCO top electrode adjacent to the YBCO/STO interface. Negative mismatch in lattice parameters of the YBCO top electrode and the STO layer is responsible for misfit dislocations at the interface as well as a high density of growth steps at the surface of the (800 nm) STO layer formed on SRO/LSATO (according to AFM data in Ref. 29) which induce a high density of stacking faults in YBCO. This may be a possible reason for the hole depletion at the interface.

Derived values of $L_{\mathrm{SRO}}$ and $L_{\mathrm{YBCO}}$ are given in Table I. They are compared with estimated values of $L_{\mathrm{LCMO}}$ (Ref. 19) and $L_{\mathrm{Ag}}$ (Ref. 18).

Concluding, we note that the electronic parameters of the interfaces between a ferroelectric layer and metallic oxide electrodes are quite sensitive to mismatch in their lattice parameters and interdiffusion of the components. Both tensile and compressive biaxial mechanical stresses in the heterostructure may promote the degradation of the ferroelectric/electrode interface microstructure as well as its stoichiometry. Those, in turn, enhance the effective penetration length of the electric field into the oxide electrode. The resulting capacitance of the heterostructure is affected, particularly at temperatures away from the Curie point, and properties like tuning are degraded. In the case of perovskite-type metallic oxide electrodes, the increase of the penetration depth will not be accompanied by a dramatic drop of the corresponding interface capacitance as the ionic contribution to the effective dielectric permittivity of the electrode near the interface is enhanced at the same time. This is one of the advantages of using ruthenates, manganites, or cuprates as thin film electrodes in epitaxial combinations with ferroelectric layers.

## ACKNOWLEDGMENTS

This study was done within the framework of the scientific cooperation between the Russian and Swedish Royal Academy of Sciences. Financial support was received from the Swedish Royal Academy of Sciences through its Nobel Institute, the Foundation of Strategic Research (SSF), the Swedish Research Council, the K.A. Wallenberg Foundation, ESF THIOX, and Project No. 04-02-16212 of the Russian Foundation of Basic Research.

[1] R. Dittmann, R. Plonka, E. Vasco, N. A. Pertsev, J. Q. He, C. L. Jia, S. Hoffmann-Eifert, and R. Waser, Appl. Phys. Lett. **83**, 5011 (2003).
[2] Yu. A. Boikov, Z. G. Ivanov, A. N. Kiselev, and E. Olsson, J. Appl. Phys. **78**, 4591 (1995).
[3] Yu Lu, X. W. Li, G. Q. Gong, G. Xiao, A. Gupta, P. Lecoeur, J. Z. Sun, Y. Y. Wang, and V. P. Dravid, Phys. Rev. B **54**, R8357 (1996).
[4] Yu. A. Boikov and T. Claeson, Phys. Solid State **43**, 2267 (2001).
[5] T. I. Kamins, J. Appl. Phys. **42**, 4357 (1971).
[6] M. Ziese, H. C. Semmelhack, K. H. Han, S. P. Sena, and H. J. Blythe, J. Appl. Phys. **91**, 9930 (2002).
[7] J. C. Jiang, W. Tian, X. Pan, Q. Gan, and C. B. Eom, Mater. Sci. Eng., B **56**, 152 (1998).
[8] R. W. G. Wyckoff, in *Crystal Structures*, 2nd ed. (Interscience, New York, 1964), Vol. 2, p. 394.
[9] J. M. Phillips, J. Appl. Phys. **79**, 1829 (1996).
[10] J.-P. Maria, H. L. McKinstry, and S. Trolier-McKinstry, Appl. Phys. Lett. **76**, 3382 (2000).
[11] E. D. Specht, R. E. Clausing, and L. Heatherly, J. Mater. Res. **5**,

2351 (1990).
[12] D. Fuchs, M. Adam, P. Schweiss, S. Gerhold, S. Schuppler, R. Schneider, and B. Obst, J. Appl. Phys. **88**, 1844 (2000).
[13] Yu. A. Boikov and T. Claecon, Physica B **311**, 250 (2002).
[14] Y. S. Vedula, V. G. Mesyats, V. V. Poplavskij, and S. I. Skuratov, Sov. Tech. Phys. Lett. **15**, 707 (1989).
[15] C. Yoshida, A. Yoshida, and H. Tamura, Appl. Phys. Lett. **75**, 1449 (1999).
[16] R. C. Neville, B. Hoeneisen, and C. A. Mead, J. Appl. Phys. **43**, 2124 (1972).
[17] A. D. Hilton and B. W. Ricketts, J. Phys. D **29**, 1321 (1996).
[18] H. Y. Ku and F. G. Ullman, J. Appl. Phys. **35**, 265 (1964).
[19] Yu. A. Boikov and T. Claeson, Phys. Rev. B **70**, 184433 (2004).
[20] P. A. Cox, R. G. Egdell, J. B. Goodenough, A. Hamnett, and C. C. Naish, J. Phys. C **16**, 6221 (1983).
[21] J. Kircher, M. K. Kelly, S. Rashkeev, M. Alouani, D. Fuchs, and M. Cardona, Phys. Rev. B **44**, 217 (1991).
[22] A. V. Boris, N. N. Kovaleva, A. V. Bazhenov, A. V. Samoilov, N.-C. Yeh, and R. P. Vasquez, J. Appl. Phys. **81**, 5756 (1997).
[23] G. Simmons, Appl. Phys. Lett. **6**, 54 (1965).
[24] C. Kittel, *Introduction to Solid State Physics*, 7th ed. (Wiley, New York, 1996), p. 148.
[25] A. G. Schrott, J. A. Misewich, V. Nagarajan, and R. Ramesh, Appl. Phys. Lett. **82**, 4770 (2003).
[26] H. Kobayashi, M. Nagata, R. Kanno, and Y. Kawamoto, Mater. Res. Bull. **29**, 1271 (1994).
[27] Yu. A. Boikov, R. Gunnarsson, and T. Claeson, J. Appl. Phys. **96**, 435 (2004).
[28] A. T. Fiory, A. F. Hebard, R. H. Eick, P. M. Mankiewich, R. E. Howard, and M. L. O'Malley, Phys. Rev. Lett. **65**, 3441 (1990).
[29] Yu. A. Boikov, D. Erts, T. Claeson, and A. Yu. Boikov, Phys. Solid State **44**, 2157 (2002).
[30] Yu. A. Boikov and V. A. Danilov, Tech. Phys. **50**, 891 (2005).